

Analytical approach for the design of flexural elements made of reinforced ultra-high performance concrete

Yiming Yao^{1,2}  | Barzin Mobasher³  | Jingquan Wang^{1,2} | Qizhi Xu²

¹Key Laboratory of Concrete and Prestressed Concrete Structures of the Ministry of Education, Nanjing, PR China

²School of Civil Engineering, Southeast University, Nanjing, PR China

³School of Sustainable Engineering and Built Environment, Arizona State University, Tempe, Arizona

Correspondence

Yiming Yao, School of Civil Engineering, Southeast University, Nanjing 211189, PR China.
Email: yiming.yao@seu.edu.cn

Funding information

National Natural Science Foundation of China, Grant/Award Number: 51908120; Natural Science Foundation of Jiangsu Province, Grant/Award Number: BK20180383; Fundamental Research Funds for the Central Universities, Grant/Award Numbers: 2242019K40079, 2242020K40099

Abstract

The increasing demands of sustainable design and construction with economical sections, reduced cover, and more efficient time schedule require more flexibility in the design methodologies. The development of ultra-high performance concrete (UHPC) have gained increasing interests as an attractive option for structural members with lightweight and superior performances. Concrete members reinforced with steel bars and fibers, generally known as hybrid reinforced concrete (HRC), offer a feasible solution in terms of reducing reinforcing materials and achieving desired structural performance. This paper proposes an analytical model to predict the flexural behavior of hybrid reinforced UHPC with steel reinforcements. Moment–curvature solutions are derived for reinforced sections based on parameterized tension-compression constitutive models. The approach is applicable to customized cross section and derivation of T-section is demonstrated. The moment–curvature response is further simplified as a tri-linear model, which is used for the development of full-range displacement solutions in analytical form. The proposed model is validated with the experimental data from literature covering a range of materials and member sizes. The full-range solutions may provide insights into the serviceability design approach based on the criterion of maximum crack width or allowable deflection.

KEYWORDS

analytical model, full-range solutions, hybrid reinforced concrete, moment–curvature, serviceability-based design, UHPC

1 | INTRODUCTION

Steel fiber reinforced concrete (SFRC) is widely used in infrastructure projects such as elevated slabs, slabs on the ground, precast tunnel lining segments.¹ Steel fibers improve the ultimate and residual tensile strength of concrete matrix, crack mitigation, and shrinkage crack

control.^{2,3} As a result, mechanical performances, durability, construction efficiency, and cost effectiveness are all improved leading to sustainable design and construction.⁴ The current practices often combines steel bars and fibers, which is known as hybrid reinforced concrete (HRC), to ensure enhanced crack resistance over the entire members and bear high localized stresses.⁵

With further development of concrete technology, ultra-high performance concrete (UHPC) is invented and has attracted great attention from engineers seeking to reduce the weight and size of structures. UHPC is a cementitious composite that exhibits excessively high compressive

Discussion on this paper must be submitted within two months of the print publication. The discussion will then be published in print, along with the authors' closure, if any, approximately nine months after the print publication.

strength (>120 MPa) and tensile strength over 7 MPa.⁶ The self-weight of UHPC structures is only 1/3 to 1/2 of RC structures.⁷ The structural performances and durability are therefore further enhanced compared to SFRC, thus the long-term economy of UHPC structures is more promising. However, field applications of UHPC are still limited since the preparation of UHPC normally requires high fiber volume fraction ($\geq 2\%$) and fine powders, which leads to complexity in preparation, construction and high costs.⁸ In addition, if steel fibers are used as the sole or primary reinforcement, significantly increased fiber dosage will be required in the whole structure to resist high stresses acting only in localized areas.⁵ As a result, hybrid reinforced UHPC containing steel bars and fibers are being studied and applied to obtain efficient structural performance with reduced fiber contents.

Computational tools provide opportunities for robust analysis of multi-variable design problems that include HRC materials since the design domain involves various material properties, cross sectional geometries, and structural response parameters in terms of stiffness, deflection, strength, and failure modes. In each category mentioned above there are discrete or continuous variables that may be specified, controlled, or allowed to vary in accordance with the design requirements. Extensive work with UHPC and greater extent of fiber reinforced concrete (FRC) has been under way to develop design guides by various research groups.^{9–13} The standard procedures normally incorporate stress–strain or stress–crack width relationship, which can be implemented in finite element (FE) and elastic–plastic solutions to develop a seamless transition among the variables that define properties, analysis, modeling, and design. Dobrusky and Chanvillard¹⁴ proposed an inverse analysis approach for UHPC flexural members utilizing moment–curvature damage model. The computation of beam equilibrium was numerically implemented with certain improvements in efficiency. Xia et al.¹⁵ proposed a size-dependent tension model to predict the ultimate moment and load–deflection response of UHPC utilizing OpenSees. The size effect was considered by means of characteristic length relating stress–crack width and stress–strain relationships.

Comparing to numerical models, analytical solutions show benefits on computational efficiency, ease implementation into design equations and analytical hand-calculation based tools for practicing engineers.^{16,17} Shafieifar et al.¹⁸ evaluated the suitability of several analytical models used in codes in predicting moment capacity of UHPC, which includes ACI 544, FHWA and ACI 318 Equations. A FE model was used while the error as much as 12% was reported. However, these methods only provide the insights into ultimate limit state (ULS) design while the remarkable advantages of UHPC compared to conventional RC often exhibit during service

limit state (SLS). Thus, the full-range solutions that keep track of load–deflection, moment–curvature, and stress–strain response are essential. Furthermore, analytical solutions for different cross sections such as rectangular, T-section and Pi-section, provide the potential for optimization on both geometries and material properties. Several analytical models have been developed by the authors and other researchers that preliminarily explore the flexural behavior of SFRC members.^{9,16,17,19,20} These models have been implemented into user-friendly excel programs and provided to users to ascertain simplicity and practicality.^{21–23} The simulation of flexural response and inverse analysis to obtain tensile properties can be done with limited number of parameters. Parametric studies on the influence of different factors can be conducted readily with easily accessible outputs.

In the present work, the overall design domain is expanded by obtaining analytical solutions for singly and doubly reinforced sections with addition of fibers. The obtained response is linearized and used as the model input to derive the analytical load–deflection equations. Correlation of constitutive response and flexural strain and stress distributions are revealed. The model is then verified with experimental data from literature, which covers various materials and beam sections including hybrid reinforced SFRC, UHPC and T-beams. Associated excel programs are developed and provided to the users.

2 | DERIVATION OF ANALYTICAL MOMENT–CURVATURE RESPONSE

Figure 1 is a schematic representation of multiple cracking in an HRC beam under flexure. The cross section is defined by $b(z)$ (discrete or continuous form) as a function of depth. The distributed cracks demonstrate tension stiffening due to longitudinal reinforcement and/or steel fibers. Non-uniform distribution of steel strain is expected as the majority tensile load across the cracks is carried by the steel bars with debonding.^{24,25} The cracked segment is represented by characteristic length L_p which may be equivalent to the crack spacing l_{cs} ,¹⁰ section height $h(z)$, length of crack a , angle of rotation $\theta(x)$, distributions of normal stress $\sigma(x,z)$, and steel strain $\epsilon_s(x,z)$. The load transfer mechanisms along the steel/concrete interfaces dictate high shear stresses where the debonding initiates. However, a smeared crack model using nominal stress–strain relationship is more suitable for multiple cracking.²⁶ Therefore the continuity of stress and strain fields is assumed to be maintained in the present model. By assuming plane section remains plane, the nominal strain at the level of steel is used to represent the average strain in reinforcements.¹⁹ For a general state of strain distribution, the location of neutral axis kh can

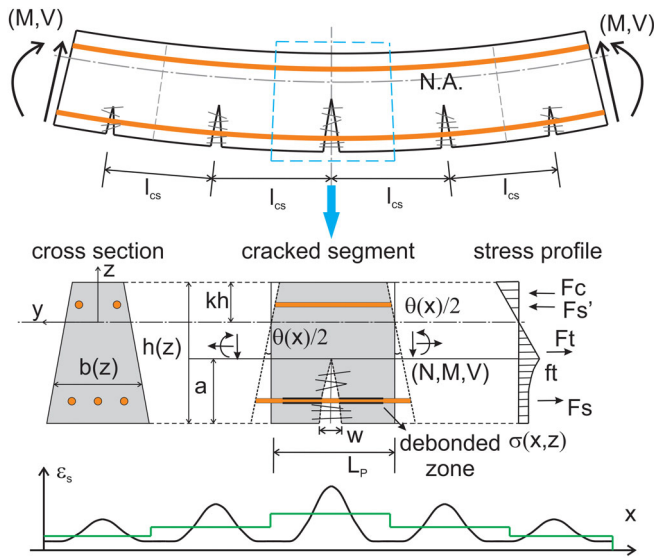


FIGURE 1 Schematic presentation of multiple cracking in an HRC beam subjected to flexural load and localized zone for a section as a nonlinear hinge

be solved by satisfying the balanced condition of axial forces. Then the formulation of moment–curvature can be obtained using the imposed strain and stress distributions in analytical form.

2.1 | Constitutive models

Piecewise compression and tension models of UHPC matrix and an elastic–perfectly plastic model for steel are used as shown in Figure 2. Note that the hardening behavior of steel can also be incorporated. The material model parameters are normalized with respect to Young's modulus E and strain at first tensile crack ϵ_{cr} . The tensile and compressive behavior of UHPC matrix are illustrated by Figure 2a,b, respectively, while the steel behavior is shown in Figure 2c. The primary material parameters include the cracking strength $\sigma_{cr} = E\epsilon_{cr}$, constant residual strength $\sigma_p = \mu\sigma_{cr} = \mu E\epsilon_{cr}$, ultimate tensile strain $\epsilon_{tu} = \beta_{tu}\epsilon_{cr}$, compressive modulus $E_c = \gamma E$, compressive strength $\sigma_{cy} = \omega\gamma\epsilon_{cr}E$ and strain $\epsilon_{cy} = \omega\epsilon_{cr}$, ultimate compressive strain $\epsilon_{cu} = \lambda_{cu}\epsilon_{cr}$, yield strain $\epsilon_{sy} = \kappa\epsilon_{cr}$ and strength $f_{sy} = \psi n\epsilon_{cr}E$ of steel. The strain for termination may be specified as needed. As shown in Figure 2d, the flange thickness t_f and web width t_w are normalized with b and h , and referred to as ζ and α , respectively. Note that $\zeta = \alpha = 1$ corresponds to a rectangular section, while both of the parameters are less than one in a T-section. The parameters of reinforcement include areas $A_s = \rho_g bh = \rho_g bd/\alpha$, $A_s' = rA_s = r\rho_g bh$, reinforced depth $d = \alpha h$. Note that the ρ_g is computed by gross sectional area bh . The constitutive models are summarized as:

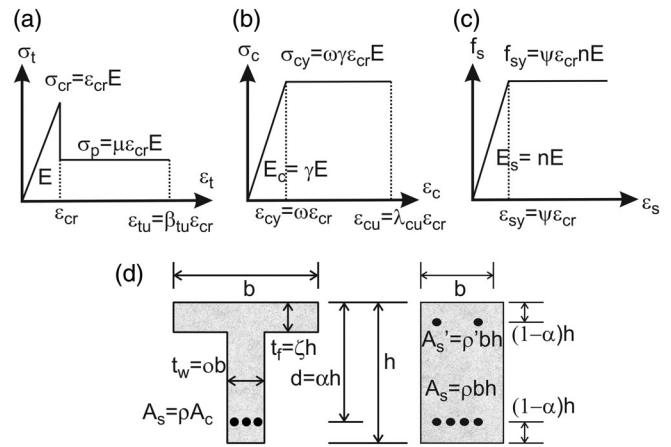


FIGURE 2 Material models for doubly reinforced concrete design (a) tension model; (b) compression model; (c) steel model; and (d) beam cross section

$$\sigma_t(\epsilon_t) = \begin{cases} E\epsilon_t & 0 \leq \epsilon_t \leq \epsilon_{cr} \\ \mu E\epsilon_{cr} & \epsilon_{cr} < \epsilon_t \leq \epsilon_{tu} \\ 0 & \epsilon_t > \epsilon_{tu} \end{cases}; \quad \frac{\sigma_t(\beta)}{E\epsilon_{cr}} = \begin{cases} \beta & 0 \leq \beta \leq 1 \\ \mu & 1 < \beta \leq \beta_{tu} \\ 0 & \beta > \beta_{tu} \end{cases} \quad (1)$$

$$\sigma_c(\epsilon_c) = \begin{cases} E_c\epsilon_c & 0 \leq \epsilon_c \leq \epsilon_{cy} \\ E_c\epsilon_{cy} & \epsilon_{cy} < \epsilon_c \leq \epsilon_{cu} \\ 0 & \epsilon_c > \epsilon_{cu} \end{cases}; \quad \frac{\sigma_c(\lambda)}{E\epsilon_{cr}} = \begin{cases} \gamma\lambda & 0 \leq \lambda \leq \omega \\ \gamma\omega & \omega < \lambda \leq \lambda_{cu} \\ 0 & \lambda > \lambda_{cu} \end{cases} \quad (2)$$

$$f_s(\epsilon_s) = \begin{cases} E_s\epsilon_s & 0 \leq \epsilon_s \leq \epsilon_{sy} \\ E_s\epsilon_{sy} & \epsilon_s > \epsilon_{sy} \end{cases}; \quad \frac{f_s(\chi)}{E\epsilon_{cr}} = \begin{cases} n\chi & 0 \leq \chi \leq \psi \\ n\psi & \chi > \psi \end{cases} \quad (3)$$

where normalized strains $\beta = \epsilon_t/\epsilon_{cr}$, $\lambda = \epsilon_c/\epsilon_{cr}$ and $\chi = \epsilon_s/\epsilon_{cr}$. Variable λ corresponding to the strain of top compressive fiber ϵ_{ctop} is used in the sectional analysis.

2.2 | Moment–curvature diagram

By assuming plane section remaining plane, linear distributions of normal strain are obtained. The corresponding profile of stresses across the section can be subsequently calculated and generated using Equations (1)–(3), as shown in Figure 3. The tensile resistance of concrete matrix after cracking is ignored in classic RC flexural design. In fact, the moment capacity of FRC systems can be considerably underestimated without considering fiber bridging mechanism.²⁷ Thus the contribution of cracked UHPC is modeled as the tensile residual strength throughout the entire tension region. In recent years, international codes and standards such as DAfStb,²⁸ RILEM TC 162-TDF,¹² CNR DT 204/2006,²⁹ EHE-08,³⁰

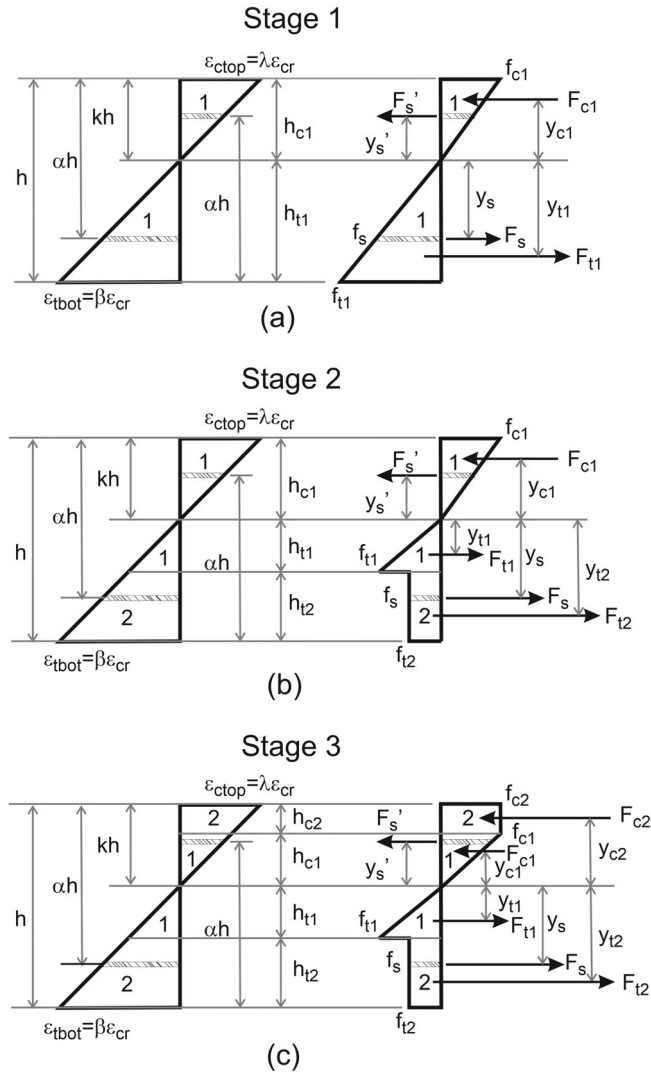


FIGURE 3 Strain and stress diagrams at three stages of applied compressive strain at top fiber (λ): (a) Stage 1 ($0 < \lambda < \lambda_{R1}$) elastic compression-elastic tension; (b) Stage 2 ($\lambda_{R1} < \lambda < \omega$) elastic compression-postcrack tension; and (c) Stage 3 ($\omega < \lambda < \lambda_{cu}$) plastic compression-postcrack tension

Model Code 2010,³¹ and ACI 544.8R³² allow for a significant residual strength in tension zone for the design using FRC. It can be obtained by standard flexural tests such as RILEM TC 162-TDF and ASTM C1609,^{12,33} or by inverse analyses.^{11,13,34,35}

Three stages of stress distributions are defined according to the interaction of tension and compression models during different stages. Figure 3a shows the elastic range Stage 1 ($0 < \lambda \leq \lambda_{R1}$) before cracking. Stage 2 ($\lambda_{R1} < \lambda < \omega$) denotes the cracked behavior in tension zone ($\varepsilon > \varepsilon_{cr}$) while the compression zone stays elastic. Stage 3 ($\omega < \lambda < \lambda_{cu}$) corresponds to the plastic range of concrete in compression. The yielding of steel causes two scenarios in Stages 2 and 3 defined as sub-stages 2.1, 2.2, or 3.1, 3.2, where the terms 1 and 2 refer to elastic and yielding of steel, respectively. The compression steel is assumed to be elastic. The heights of compression and tension zones, moment arm, stress vertices and force terms are presented in Tables A.1 and A.2.

The location of neutral axis kh is obtained by solving force equilibrium. Due to the nature of linearized stress distributions, quadratic forms of the equilibrium equations are constructed without higher order terms. Internal moment is obtained as the integration of the first moment of normal stresses about the neutral axis. Secant stiffness in flexure is obtained in each step of λ as the ratio of moment to curvature. The normalized moment, curvature and secant stiffness are shown in Equation (4):

$$\begin{aligned} M_i &= m_i M_{cr}; & M_{cr} &= \frac{1}{6} b h^2 E \varepsilon_{cr} \\ \varphi_i &= \kappa_i \varphi_{cr}; & \varphi_{cr} &= \frac{2 \varepsilon_{cr}}{h} \\ K_i &= K_i' K_{cr}; & K_{cr} &= \frac{1}{12} b h^3 \end{aligned} \quad (4)$$

The normalized moment and location of neutral axis are presented in Table 1. To identify the transition from elastic stage to cracked stage, the critical value of the compressive strain λ_{R1} is solved at the level of cracking:

$$\frac{\lambda_{R1} \varepsilon_{cr}}{kh} = \frac{\varepsilon_{cr}}{(1-k)h} \quad (5)$$

The expression k_1 in Table 1 is adopted for k , and λ_{R1} is solved as:

$$\lambda_{R1} = \begin{cases} -\frac{1 + n \rho_g r + n \rho_g - \sqrt{(n \rho_g r + n \rho_g + 1)^2 - (\gamma - 1) [2 n \rho_g (a r - \alpha - r) - 1]}}{2 + n \rho_g r + n \rho_g + \sqrt{(n \rho_g r + n \rho_g + 1)^2 - (\gamma - 1) [2 n \rho_g (a r - \alpha - r) - 1]}} & \text{when } \gamma \neq 1 \\ -\frac{2 n \rho_g (r \alpha - \alpha - r) - 1}{2 n \rho_g (r \alpha - \alpha + 1) + 1} & \text{when } \gamma = 1 \end{cases} \quad (6)$$

TABLE 1 Normalized neutral axis and moment solutions for rectangular section

Stage	k	m
1 ^a	$k_1 = \frac{A_1 + \sqrt{A_1^2 - (\gamma - 1)(A_2 - 1)}}{\gamma - 1}$	$mm_1 = B_1 k^2 + B_2 k + B_3 - 6\lambda + \frac{B_4 + 2\lambda}{k}$
2.1	$k_{21} = \frac{A_3 + \sqrt{A_3^2 - A_2 A_4 \lambda}}{A_4}$	$mm_{21} = B_5 k^2 + B_6 k + B_3 + \frac{B_4}{k}$
2.2	$k_{22} = \frac{A_5 + \sqrt{A_5^2 - A_4 A_6 \lambda}}{A_4}$	$mm_{22} = B_6 k^2 + B_7 k + B_8 + \frac{B_9}{k}$
3.1	$k_{31} = \frac{A_3 + \sqrt{A_3^2 - A_2 A_7 \lambda}}{A_7}$	$mm_{31} = B_{10} k^2 + B_{11} k + B_3 + 3\mu + \frac{B_4}{k}$
3.2	$k_{32} = \frac{A_5 + \sqrt{A_5^2 - A_6 A_7 \lambda}}{A_7}$	$mm_{32} = B_{10} k^2 + B_7 k + B_8 + \frac{B_9}{k}$

$$^a k_1 = \frac{A_2 - 1}{2A_1}, \quad mm_1 = B_2 k + B_3 - 6\lambda + \frac{B_4 + 2\lambda}{k} \text{ when } \gamma = 1.$$

Balanced reinforcement ratio $\rho_{g,bal}$ is an important parameter in the flexural design to avoid undesired modes of failure. The analytical form of moment enables the derivation of the equation for $\rho_{g,bal}$, which is another benefit of the proposed model. Balanced failure represents the simultaneous state of concrete compression failure and steel yielding ($\epsilon_c = \epsilon_{cu}$ and $\epsilon_s = \epsilon_{sy}$), which can be characterized by the following equation:

$$\frac{\lambda_{cu} \epsilon_{cr}}{kh} = \frac{\psi \epsilon_{cr}}{(\alpha - k)h} \quad (7)$$

Thus $\rho_{g,bal}$ can be solved by substituting k_{32} from Table 1:

$$\rho_{g,bal} = \frac{\alpha[\alpha\omega\gamma(\omega - 2\lambda_{cu}) + 2\mu(\psi - \alpha) + 2\mu\lambda_{cu}(1 - \alpha) + \alpha]}{2n[\psi^2(r\alpha - r - \alpha) + \psi\lambda_{cu}(3r\alpha - 2r - \alpha) + r\lambda_{cu}^2(2\alpha - 1)]} \quad (8)$$

For singly reinforced section with tensile reinforcements only, that is, $r = 0$, Equation (8) is simplified to:

$$\rho_{g,bal} = \frac{2\mu(\lambda_{cu}(\alpha - 1) + \alpha - \psi) + \alpha\gamma\omega(2\lambda_{cu} - \omega) - \alpha}{2n\psi(\lambda_{cu} + \psi)} \quad (9)$$

which is exactly the solution obtained by Mobasher et al.¹⁹ Similarly, moment capacity for under-reinforced section ($\rho_g < \rho_{g,bal}$) can also be derived. By imposing L'Hopital's rule, ultimate moment M_u is approximated at infinite compressive strain ($\lambda \rightarrow \infty$) when the failure of concrete compression $\lambda = \lambda_{cu} = \infty$. Normalized moment capacity m_∞ , can then be obtained from the expression of m_{32} :

$$m_u = m_\infty = \lim_{\lambda_{cu} \rightarrow \infty} m_{32} = \frac{3(G_1 - G_2 - \mu\omega\gamma)}{\omega\gamma + \mu} \quad (10)$$

$$M_u = m_u M_{cr} = \frac{3(G_1 - G_2 - \mu\omega\gamma)}{\omega\gamma + \mu} M_{cr}$$

$$\text{where } G_1 = 2\psi n \rho_g [\omega\gamma(r\alpha - r + \alpha) + \mu(r\alpha + \alpha - 1)],$$

$$G_2 = [\psi n \rho_g (r - 1)]^2.$$

2.3 | Moment-curvature equations for T-beams ($\alpha \neq 1, \zeta \neq 1$)

Flanged sections are also widely used in engineering applications, such as the beam-slab system, bridge girder, and recently developed UHPC pi-girder.³⁶ The flanged sections made of UHPC can be optimized to reduce the self-weight and material use without compromising the bending properties. To model the UHPC Pi-girder³⁶ and SFRC roof elements³⁷ with present approach, the sections may be converted into standard T-beam or inverted T-beam with equivalent flexural stiffness. Analytical based design procedure can therefore be developed besides numerical modeling.

Using the same constitutive models as shown in Figure 2, the strain and stress profiles of T-section are shown in Figure 4. The compressive force contributed by the web section is ignored for simplicity as the major contribution is provided by the flange section (shown as the shaded region in Figure 4a). The heights of compression and tension zones, moment arm, stress vertices and force terms are presented in Tables A.3 and A.4.

Same procedure of moment-curvature analysis is performed to derive the analytical solutions. The normalized moment and location of neutral axis of each stage are presented in Table 2. However, note that M_{cr} of a T-section is different from that of the rectangular beam ($M_{cr} = bh^2 E \epsilon_{cr} / 6$). Exact expression of cracking moment increases the complexity of the solutions. Parametric studies³⁸ showed that the M_{cr} is marginally affected by the flange thickness ζ , but almost linearly related to the web thickness o . Therefore, by assuming that the cracking moment is a linear function of o in a range from 0.05

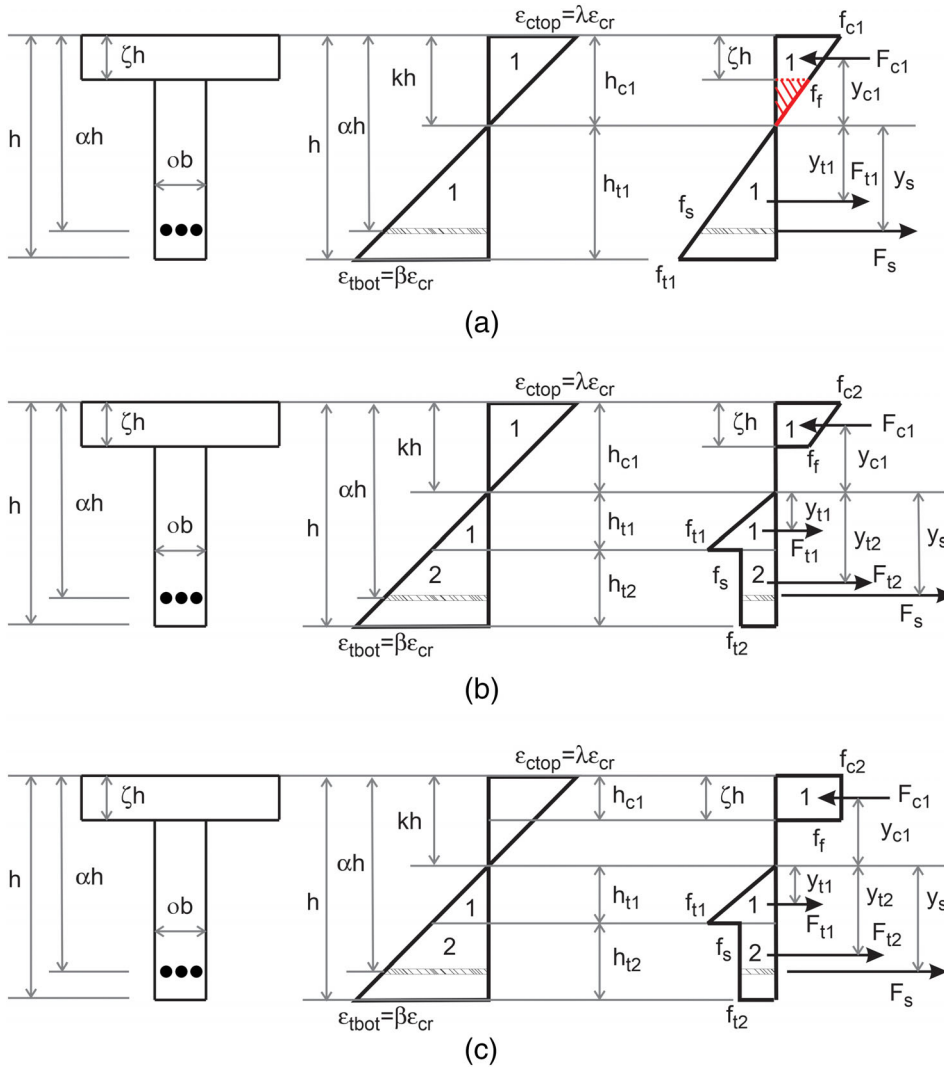


FIGURE 4 Strain and stress diagrams at three stages of applied compressive strain at top fiber (λ): (a) Stage 1 ($0 < \lambda < \lambda_{R1}$) elastic compression-elastic tension; (b) Stage 2 ($\lambda_{R1} < \lambda < \omega$), elastic compression-postcrack tension; and (c) Stage 3 ($\omega < \lambda < \lambda_{cu}$) plastic compression-postcrack tension

TABLE 2 Normalized neutral axis and moment solutions for T-section

Location of neutral axis	Stage	k	m
Web	1	$k_1 = \frac{C_1 - \sqrt{C_1^2 - 4\alpha C_2}}{2\alpha}$	$mm_1 = \frac{200\lambda(\alpha k^3 + 3C_1 k^2/2 - 3C_2 k + D_1)}{3(40\alpha + 1)k}$
	2.1	$k_{21} = \frac{C_3 + \sqrt{C_3^2 - 4C_4 C_5}}{2C_4}$	$mm_{21} = \frac{100(D_2 k^3 + D_3 k^2 + D_4 k + D_5)}{(40\alpha + 1)k}$
	2.2	$k_{22} = \frac{C_6 + \sqrt{C_6^2 - 4\lambda^2 \zeta \gamma C_4 C_9}}{2C_4}$	$mm_{22} = \frac{100(D_2 k^3 + D_6 k^2 + D_7 k + D_8)}{(40\alpha + 1)k}$
	3.1	$k_{31} = \frac{C_3 + \sqrt{C_3^2 - 4C_5 C_7}}{2C_7}$	$mm_{31} = \frac{100(D_9 k^3 - D_3 k^2 - D_4 k - D_5)}{(40\alpha + 1)k}$
	3.2	$k_{32} = \frac{C_6 + \sqrt{C_6^2 - 4\lambda^2 \zeta \gamma C_7 C_9}}{2C_7}$	$mm_{32} = \frac{100(D_9 k^3 + D_6 k^2 + D_7 k + D_8)}{(40\alpha + 1)k}$
Flange	1	$k_1 = \frac{E_1 + \sqrt{E_1^2 - 4\gamma E_2}}{2\alpha}$	$mm_1 = \frac{200\lambda(\lambda k^3 - 3E_1 k^2/2 + 3E_2 k + F_1)}{3(40\alpha + 1)k}$
	2.1	$k_{21} = \frac{E_3 + \sqrt{E_3^2 - 4E_4 E_5}}{2E_4}$	$mm_{21} = \frac{100(F_2 k^3 + F_3 k^2 + F_4 k + F_5)}{(40\alpha + 1)k}$
	2.2	$k_{22} = \frac{E_6 + \sqrt{E_6^2 - 4E_4 E_7}}{2E_4}$	$mm_{22} = \frac{100(F_2 k^3 + F_6 k^2 + F_7 k + F_8)}{(40\alpha + 1)k}$
	3.1	$k_{31} = \frac{E_3 + \sqrt{E_3^2 - 4E_5 E_8}}{2E_8}$	$mm_{31} = \frac{100(F_9 k^3 - F_3 k^2 - F_4 k - F_5)}{(40\alpha + 1)k}$
	3.2	$k_{32} = \frac{E_6 + \sqrt{E_6^2 - 4E_7 E_8}}{2E_8}$	$mm_{32} = \frac{100(F_9 k^3 + F_6 k^2 + F_7 k + F_8)}{(40\alpha + 1)k}$

to 0.30, a least square fit on the exact solutions yields the equation:

$$M_{cr} = \left(\frac{0}{5} + \frac{1}{200} \right) b h^2 E \varepsilon_{cr} \quad (11)$$

The balanced reinforcement ratio is derived in a similar manner:

$$\rho_{g,bal} = - \frac{2\zeta\gamma\omega(\psi + \lambda_{cu}) + 2\mu\lambda_{cu}(\alpha - 1) + 2\mu\alpha(\alpha - \psi) - \alpha\omega}{2n\psi(\zeta\alpha - \zeta - \alpha)(\lambda_{cu} + \psi)} \quad (12)$$

Full-range moment–curvature diagrams can then be constructed by implementing the derived equations using computer codes such as Matlab, excel or other programs. Figure 5 represents a superposition of various moment–curvature curves of individual modes of loading. Note that each range is operative in the domain of evaluation as a function of λ . The intersection of any two modes indicates that solutions are available for both assumptions. Therefore, it is likely that a switch over from one mode to another would take place at the intersection point and the mode with the lower magnitude of bending moment at a given curvature will dominate the response. Based on the above, one can develop the compound moment–curvature diagram by obtaining an envelope of the interacting modes. As a follow-up, this response can be used either in a multi-nonlinear closed-form solution numerically or interpolated into simplified bilinear-or trilinear model that will be presented in the next section.

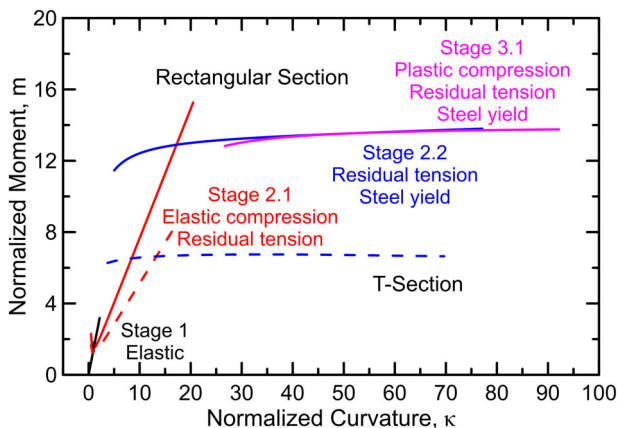


FIGURE 5 Superposition of various moment–curvature response curves obtained from individual mode of loading

3 | DERIVATION OF LOAD–DEFLECTION SOLUTIONS

3.1 | Linearized moment–curvature model

The derivations of load–deflection response involve two types of methods, which are numerical integration using moment-area method,¹¹ and closed-form solutions based on linearized moment–curvature model presented by the authors.¹⁷ The time efficiency of the latter approach was substantially improved and the computational costs related to section integration was avoided. In other words, by taking moment–curvature relationship as the model input, one can obtain load–deflection response analytically for arbitrary combination of cross section geometries and materials.

Figure 6 is a schematic of the linearization procedure of moment–curvature model. The trilinear response consists of linear-elastic stage, postcracking stage with a reduced flexural stiffness EI_{cr} , and perfect plasticity stage corresponding to the yielding in tensile reinforcement. The trilinear curve is governed by first flexural cracking (M_{cr}, φ_{cr}) and tensile steel yielding (M_p, φ_p), which are normalized as (1,1) and (κ_p, m_p) , respectively. The plastic stage is terminated at a limit state criterion such as maximum curvature, or the curvature corresponding to a strain limit. The full-range curve can be represented by the following equations:

$$m(\kappa) = \frac{M(\varphi)}{M_{cr}}, \quad \kappa = \frac{\varphi}{\varphi_{cr}}, \quad m_p = \frac{M_p}{M_{cr}}, \quad \kappa_p = \frac{\varphi_p}{\varphi_{cr}} \quad (13)$$

$$\begin{aligned} m(\kappa) &= \kappa & 0 < \kappa \leq 1 \\ m(\kappa) &= \frac{m_p - 1}{\kappa_p - 1}(\kappa - 1) + 1 & 1 \leq \kappa \leq \kappa_p \\ m(\kappa) &= m_p & \kappa_p \leq \kappa \leq \kappa_{max} \end{aligned} \quad (14)$$

To derive the load–deflection solutions, moment and curvature distributions for a certain beam configuration are required for uncracked and cracked scenarios. Piecewise linear distributions of curvature along the beam at different stages are derived from bending moment and the trilinear moment–curvature relationship, see Figure 7 for the case of four-point bending (4 PB). Two stages are identified including the linear elastic stage where $0 \leq M(L/2) \leq M_{cr}$ (Stage 1), and the cracked stage where a section of the beam exceeds M_{cr} (Stage 2). The analytical equations of load–deflection are derived by integration of curvature along the entire beam, where the constant terms are evaluated by imposing continuity in displacement fields and the

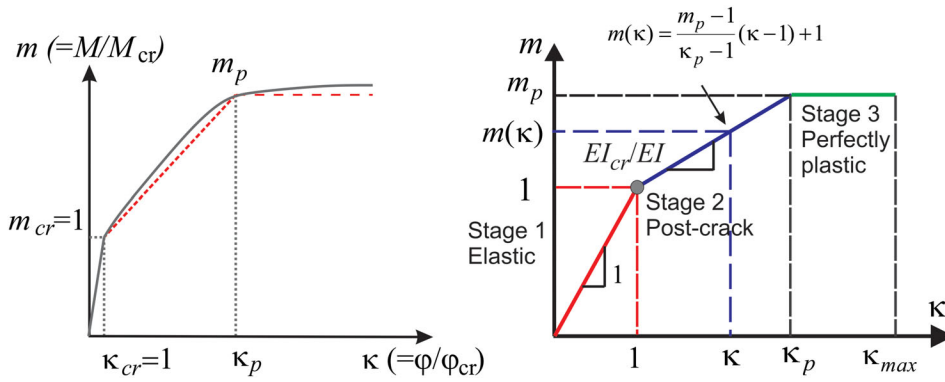


FIGURE 6 Linearization of moment-curvature diagram and the proposed trilinear model defined by normalized parameters

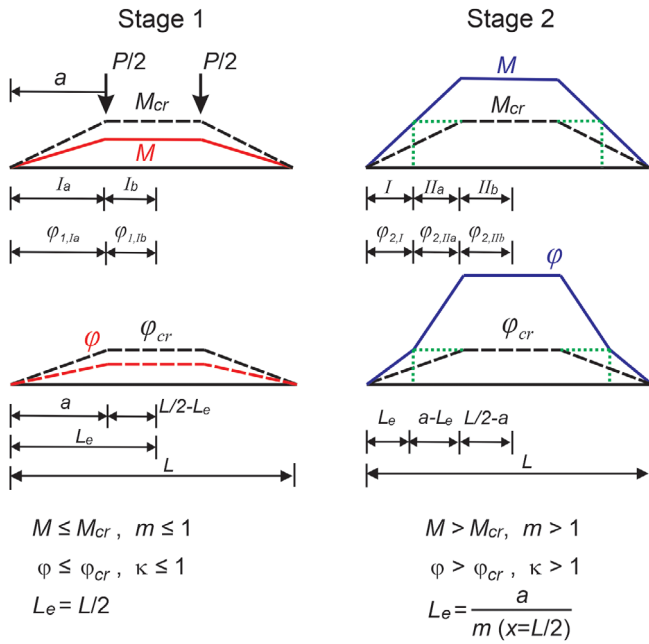


FIGURE 7 Moment and curvature distributions in Stages 1 and 2 for a beam under 4 PB

boundary conditions. Full-range profiles of rotation and deflection as a function of applied load and location are obtained.

This approach has been extended to different combinations of beam types and applied loads such as cantilever, over-hang, distributed load with detailed derivations in.^{17,39} Besides the analytical moment-curvature relationships for rectangular and T-sections in this study, one can also perform sectional analysis using any available program for standard or customized cross section such as circular, hollow, I-section etc. as input to the load deflection analysis. A key advantage of using analytical solutions is their applicability for routines of sectional optimization considering the material properties and geometries since response surfaces can be generated as needed.

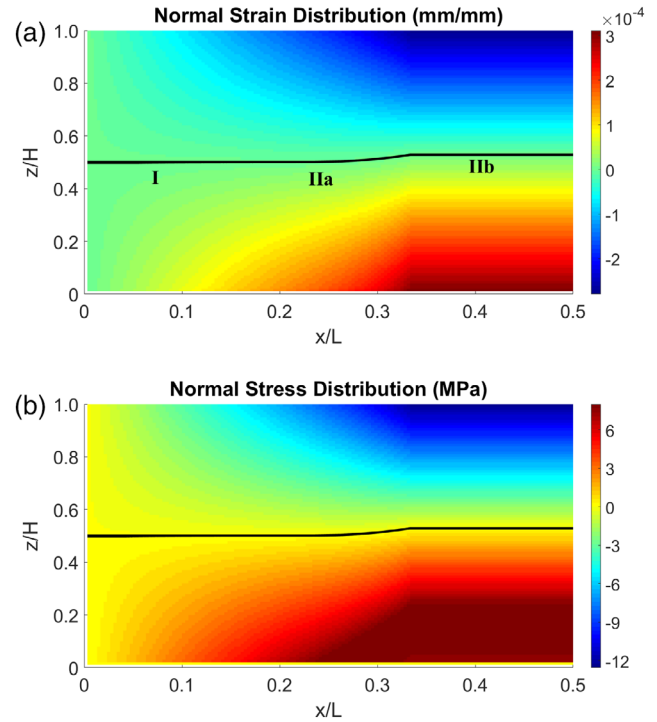


FIGURE 8 Distributions of (a) normal strain and (b) normal stress of a 4 PB ($L = 450$, $b = 150$, $d = 150$ as dimensions in mm, $E = 45$ GPa, $\epsilon_{cr} = 0.000178$)

3.2 | Correlation of constitutive response and flexural strain and stress distributions

The displacements and constitutive models in this study are linked by the analytical solutions of moment, curvature, and neutral axis. Full field deflections and rotations can be combined with the solution of neutral axis location to obtain 2-D strain and stress distributions or contour plots at various levels of load or deformation.

A case study is presented as demonstration based on a plain UHPC beam with span $L = 450$, beam width $b = 150$, and beam height $h = 150$ (in mm). Typical material parameters of UHPC were used including $E = 45$ GPa, $\epsilon_{cr} = 0.000178$, $f'_c = 150$ MPa, $\epsilon_{cu} = 0.0045$, $\epsilon_{tu} = 0.03$,

$\mu = 0.6$, $\omega = 18.7$, $\lambda_{cu} = 25.3$, $\beta_{tu} = 168.5$, $\gamma = 1$. Figure 8 shows the distributions of normal strain and stress in the cracked stage for half of a 4 PB beam due to symmetry. The distributions were selected an intermediate loading stage of 80% peak load. The solid line indicates the location of the neutral axis path from elastic to cracked section as it progresses towards the compression zone with increasing load. The corresponding normal stress distribution is illustrated in Figure 8 allowing a direct analytical correlation of internal stress and strain distributions with the constitutive material properties and the load–deflection response.

The implementation of serviceability-based design approach requires the criteria based on service load level and deformation, which can be obtained from the present distributions of deflection, curvature or strain at a specific point. For instance, the normalized deflections as a function of location are represented as deformation envelope at loading levels of 20%, 40%, 60%, 80%, and 100% of maximum applied load, see Figure 9. In addition to load–position interaction, any other combinations of stress, strain and curvature can be used to form either deformation envelopes at required level of serviceability states or continuous response surfaces. Design charts can then be constructed for the selection of design parameters.

4 | EXPERIMENTAL VALIDATION

4.1 | Model validation with experimental data

The proposed approach is applicable to combinations of various materials and cross sections at different scales. In

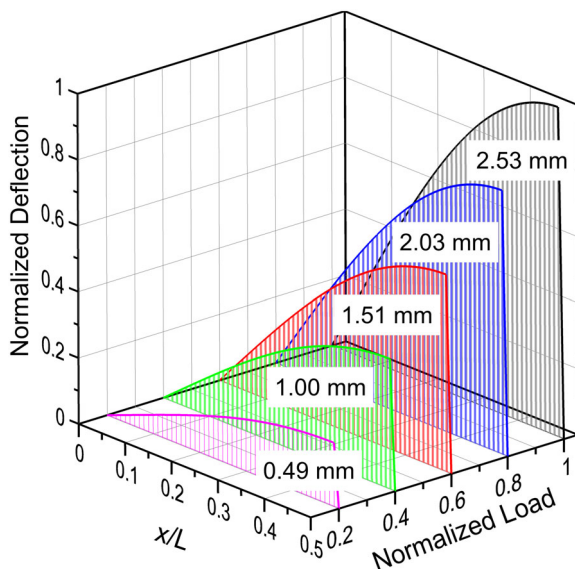


FIGURE 9 Deflection distributions at different loading levels for 4 PB (the maximum displacement values for each load level are indicated)

this section, the model was evaluated by simulating experimental results from literature on different materials and sections. As mentioned previously, numerical integration and linearized moment–curvature model can be used to compute load–deflection response, which are both demonstrated in this section. The linearized moment–curvature model was applied to rectangular beams while the numerical integration method was used for T-beams. The first set of data are obtained from the studies performed by Gribniak et al.^{13,40} Flexural tests of SFRC beams reinforced with steel or GFRP bars were conducted and moment–curvature response curves were presented. The beams have a span of 3,000 mm, height ranging from 298 mm to 304 mm, and width ranging from 270 mm to 285 mm. The strength of concrete, steel and GFRP bars are listed in Table 3. Note that the parameter γ was assumed to be 1 for all the case studies. The simulated moment–curvature diagrams are shown in Figure 10 for different fiber volume fractions and types of longitudinal reinforcements. It is observed that the model predictions perform better at higher load levels and fiber volume fractions. The experimental data were underestimated when the fiber volume fraction is lower. It may be traced back to the drop-down residual strength used in the proposed model such that the tensile contribution by UHPC after cracking is omitted, which leads to conservative predictions. As μ increases, this phenomenon is diminished and deflection hardening behavior occurs at lower load levels.

Oh²⁷ investigated the flexural performances of full-scale beams with addition of steel fibers from 0% to 2% by volume. The beam specimens tested under 4 PB have a cross section of 180 mm \times 120 mm, and span of 1,800 mm. The compressive strength of different mixes ranged from 40.3 to 47.8 MPa, and the split tensile strength increased from 3.1 to 8.1 MPa from plain concrete to 2% of steel fiber addition. Longitudinal reinforcement ratio for the singly and doubly reinforced sections were 1.84% and 2.65%, respectively. The used model parameters are summarized in Table 3. Figure 11 compares the experimental and simulated load–deflection curves of the HRC beams. The postcracking moment capacity and flexural stiffness in excess of 20% in this case as a result of increasing reinforcement ratio. On the other hand, the effects of steel fibers on increasing the moment capacity for each group of beams is also observed, which is simulated by increasing μ . Further discussions on the effects of ρ_g and μ will be discussed in the next section on parametric study.

Yang et al.⁴¹ conducted 4 PB tests on hybrid reinforced UHPC beams with 2% of steel fiber, with the beam cross section of 180 mm \times 270 mm and span of 2,700 mm. Compressive strength over 190 MPa was

TABLE 3 Material properties and model parameters for experimental verification studies of rectangular beams

Study	ρ (%)	v_f (%)	f'_c (MPa)	E (GPa)	E_s (GPa)	f_{sy} (MPa)	ϵ_{cr} ($\mu\epsilon$)	ω	ψ	μ	α	λ_{cu}	m_p	κ_p	κ_{max}
Gribniak et al. (2012) ^a	0.3	0	50.9	33.5	209	578	133	11.4	20.8	0.2	0.90	26.4			
		0.5	55.6	35.0	203	560	126	12.6	22.0	0.43	0.92	27.8			
		1	48	32.6	203	560	137	10.8	20.2	0.52	0.91	25.6	—		
		1.5	52.2	34.0	203	560	132	11.6	20.9	0.63	0.91	26.5			
Gribniak et al. (2013) ^a	0.6 (GFRP) 0.6 (GFRP)	0	48.1	32.6	210	632	105	14.1	28.7	0.1	0.91	42.9			
		1	56	35.2	65.1	1,468	110	14.4	204.6	0.25	0.81	29.9	—		
		1	56	35.2	64.4	1,336	123	13.0	169.1	0.25	0.80	20.4			
		0	40.3	23.8			104	13.0	20.2	0		24.5	13.6	27.7	47.2
Oh. (1992)	1.84	1	43.0	24.7			175	7.9	12.0	0.2		17.2	8.2	16.5	31.2
		2	47.8	24.7	200	420	263	5.3	8.0	0.4	0.78	21.1	5.7	11.5	40.2
		0	40.3	23.8			104	13.0	20.2	0		42.1	9.9	25.2	79.1
		1	43.0	24.7			175	7.9	12.0	0.2		33.1	6.1	14.8	59.4
Yang et al. (2010)	0.60 0.90	2	47.8	24.7			249	5.3	8.0	0.4		20.4	4.6	11.1	34.5
		2	192.2	46.7	200	600	384	10.7	7.8	0.55	0.87	11.7	2.5	7.6	9.6
			196.1	45.5			384	11.2	7.8	0.55	0.87	11.7	2.9	8.0	14.4

^aExperimental moment–curvature response curves were provided by the authors such that the m_p , κ_p , κ_{max} were not required in the simulations.

obtained with elastic modulus ranging from 45.5 to 45.8 GPa. Strain gages were attached at the mid-span along the depth of the beam, as well as the tensile steel bars, which allowed extraction of a strain profile and curvature calculations. Figure 12 compares both the moment–curvature and load–deflection response curves of the UHPC beams at two levels of ρ_g (0.6% and 0.9%).

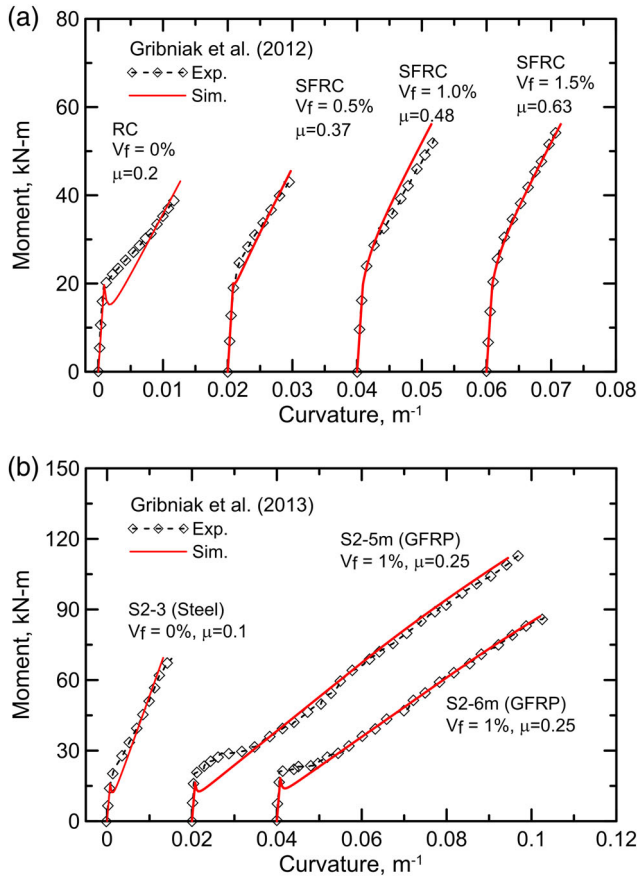


FIGURE 10 Comparison between experimental and simulated moment–curvature response curves for (a) steel reinforced SFRC beams by Gribniak et al.¹³ and (b) steel/GFRP reinforced SFRC beams by Gribniak et al.⁴⁰

Similarly, increases in moment capacity and postcracking stiffness with increasing ρ_g were observed in the experiment and captured by the model. The accurate prediction of the moment–curvature response verifies the algorithm of the analytical moment–curvature solutions. Figure 13 illustrates the results from strain gauge measurements in terms of the strain near extreme compressive fiber and the strain in tensile steel bars. The location of neutral axis is computed using the assumption of plane section remains plane. On the other hand, the analytical model keeps tracking the normal strains along the depth of the cross section and neutral axis location. The moment versus both compressive and tensile strains are presented in comparison with experimental results. The model is able to fit both strains and depth of neutral axis during loading process. The constitutive material models described by stress–strain relationship are linked to load–deflection response by moment–curvature behavior in the present model. Thus, the comparisons between experiment and simulated results in this case study validate the proposed methodology in terms of both local behavior of a cross section and global behavior of a beam element.

The solutions for T-section are verified with the flexural data of SFRC beam by Abdu-Ahad and Aziz⁴² with a span of 1800 mm, and UHPC beam by Qi et al.⁴³ with a span of 1,140 mm, and UHPC beam by Qiu et al.⁴⁴ with a span of 3,500 mm. The cross sectional parameters of the reinforced SFRC beam with 2% of steel fiber include $b = 250$ mm, $t_w = 100$ mm, $h = 210$ mm and $t_f = 60$ mm, therefore the ζ and ϕ equal to 0.29 and 0.4, respectively. Concrete compressive strength is 18.8 MPa. The UHPC beam of second case was cast with 2% of steel fibers where a compressive strength of 116 MPa was obtained. Geometries of cross section include $b_f = 120$ mm, $b_w = 40$ mm, $h = 140$ mm and $t_f = 35$ mm, thus the parameters ζ and ϕ are 0.25 and 0.33, respectively. The third set is low-profile T-beam with cross section of

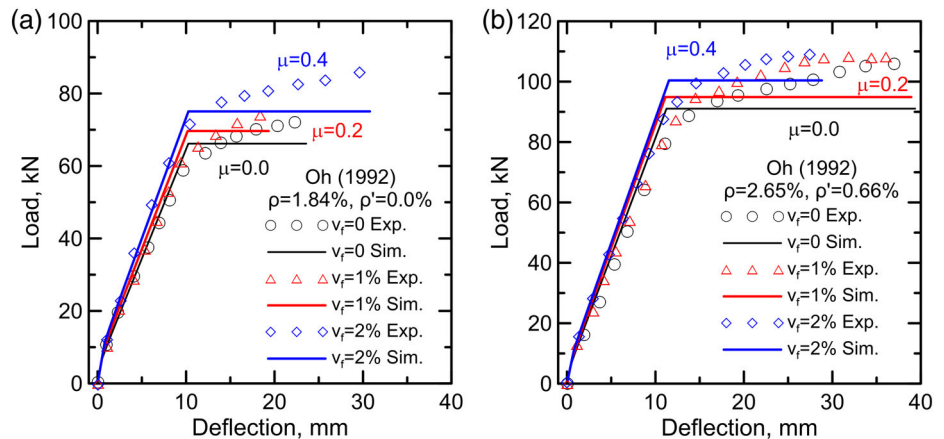


FIGURE 11 Comparison between experimental and simulated load–deflection curves for the beams with reinforcement ratio of (a) 1.84% and (b) 2.65% from Oh²⁷

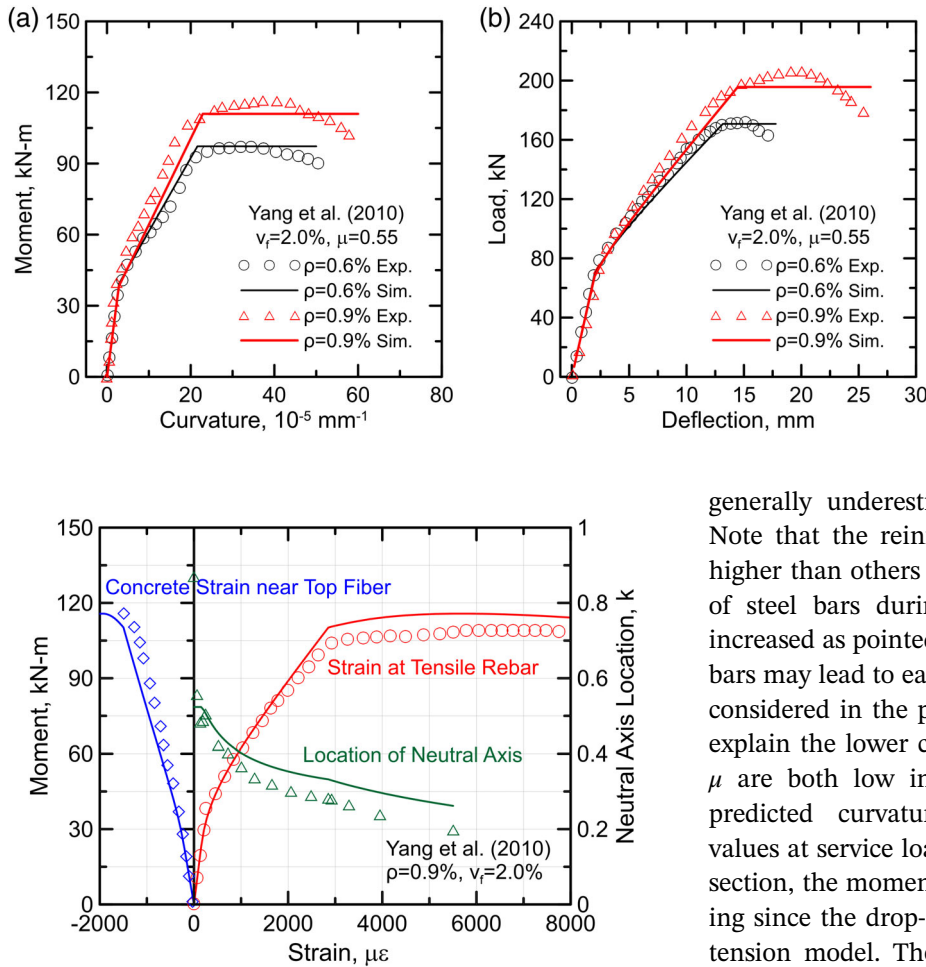


FIGURE 13 Comparison between experimental and simulated responses of normal strains near extreme compressive fiber, at tensile steel and location of neutral axis

$b = 700$ mm, $t_w = 180$ mm, $h = 220$ mm and $t_f = 80$ mm, resulting in ζ of 0.36 and α of 0.26. The compressive is 131.6 MPa and Young's Modulus is 44 GPa. Volume fraction of steel fiber is 2% and two reinforcement ratios were investigated including 0.73% and 1.14%. Other model parameters are summarized in Table 4. Experimental and simulated load–deflection response curves are compared in Figure 14, where well agreement is observed.

Error analysis was conducted to quantitatively evaluate the accuracy of the model predictions. Flexural deformations (curvature or deflection) of the beams from all the case studies were investigated at reference load levels. The two reference load levels selected include the ultimate state P_{ult} (M_{ult}) corresponding to yielding of tensile steel strength of steel reinforcement, and the service load P_{ser} (M_{ser}) which was assumed to be 0.55 of ultimate load.⁴⁰ Note that these loading levels are the computed values instead of experimental. The prediction errors are summarized in Table 5. It can be seen that the deflections by Oh,²⁷ Qi et al.⁴³ and Abdul-Ahad and Aziz⁴² are

FIGURE 12 Comparison between experimental and simulated results of (a) moment–curvature and (b) load–deflection from Yang et al.⁴¹

generally underestimated, especially for ultimate load. Note that the reinforcement ratios of these studies are higher than others such that the contribution proportion of steel bars during the loading procedure might be increased as pointed out in.⁴⁵ Higher load carried by steel bars may lead to earlier debonding while this effect is not considered in the proposed model, which could possibly explain the lower calculated deformations. When ρ_g and μ are both low in the case by Gribniak et al.,¹³ the predicted curvatures overestimate the experimental values at service load levels. As discussed in the previous section, the moment shows sudden decreases after cracking since the drop-down residual strength is used in the tension model. The contribution of concrete tension is therefore omitted which is more notable at low reinforcement ratio.

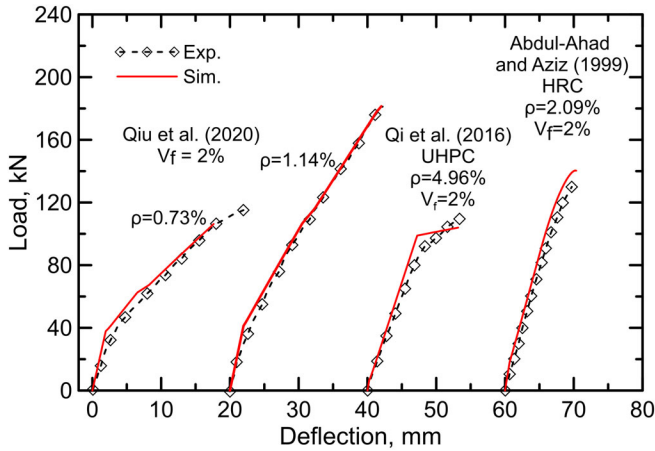
4.2 | Model validation with FE analysis

To further validate the proposed model, two sets of data by Yang et al.⁴¹ and Qiu et al.⁴⁴ were simulated by FE analysis. The FE model was established by software ABAQUS 6.14 and standard computing mode was adopted. In the FE model, UHPC beam, loading plates and support plates were all simulated through C3D8R elements, which is commonly used for solid members. The longitudinal and transvers bars were modeled by truss elements T3D2. The steel reinforcement cage was embedded in UHPC beam while the loading and support plates were restricted with the UHPC part via tie constraints. Load was applied to referencing points coupling on the loading plates. The boundary conditions include horizontal and vertical translation constraints introduced at one support and vertical translation constrain applied at the other.

The uniaxial stress–strain relationship of steel reinforcement was characterized by Young's modulus E_s and Poisson's ratio ν . The plastic behavior was defined as

TABLE 4 Material properties and model parameters for experimental verification studies of T beams

Study	ρ (%)	v_f (%)	f'_c (MPa)	E (GPa)	E_s (GPa)	f_{sy} (MPa)	ε_{cr} ($\mu\epsilon$)	ω	ψ	μ	α	ϕ	ζ	λ_{cu}
Qiu et al. (2020)	0.73	2	131.6	44	200	460	205	14.6	10.1	0.55	0.84	0.26	0.36	26.9
	1.14													
Abdul-Ahad and Aziz (1999)	2.09	2	18.8	20.4	200	465	210	5.9	11.1	0.3	0.81	0.4	0.29	40.9
Qi et al. (2016)	4.96	2	116	36.5	200	761	140	22.7	27.2	0.3	0.81	0.33	0.25	25.0

**FIGURE 14** Comparison between experimental and simulated load-deflection responses of HRC beams by Abdul-Ahad and Aziz,⁴² Qi et al.,⁴³ and Qiu et al.⁴⁴

linear hardening by specifying plastic stress and strain. The material properties were taken from the experimental data by the authors.^{41,44} Concrete damage plasticity (CDP) model was used for UHPC. The parameters include dilation angle of 56, eccentricity 0.1, stress ratio 1.1, shape factor 0.667, viscosity parameter 0.005. For the purpose of model validation, the linearized compression and tension relations used in the proposed analytical model (Tables 3 and 4) were employed for the FE simulation. The FE results were compared with experimental data and analytical predictions as shown in Figure 15, where good agreement is observed.

5 | PARAMETRIC STUDIES

The main advantage of analytical solutions is that parametric studies on primary factors such as μ and ρ_g can be easily performed. To demonstrate the effects of fibrous and steel reinforcements, a material model with typical UHPC properties is used, which include $E = 45$ GPa, $\varepsilon_{cr} = 0.000125$, $f'_c = 150$ MPa, $\varepsilon_{cu} = 0.0045$, $\varepsilon_{tu} = 0.03$, $E_s = 200$ GPa, $f_{sy} = 500$ MPa, reinforcement depth $d = 0.9 h$. The corresponding model parameters are $\gamma = 1$,

$\omega = 18.7$, $\lambda_{cu} = 25.3$, $\beta_{tu} = 169$, $\psi = 14.0$, $n = 4.4$, $r = 1$ and $\alpha = 0.9$. The two changing variables are $0.0 \leq \mu \leq 1.0$, and $0.0 \leq \rho_g \leq 0.015$, which represent a wide range of fiber dosages and reinforcement ratio.

Figure 16 illustrates the normalized moment-curvature and stiffness degradation with changing μ , ρ_g , and f_{sy} . Scenarios including first cracking, tension steel yielding and plasticity of compression concrete are identified on the curves. As ρ_g increases from 0 to 0.015, significant improvements in moment capacity and cracked flexural stiffness are observed, which represent the transition from plain SFRC to an HRC section, see Figure 16a. It is also observed that the plastic stage of compression concrete occurs earlier with increasing ρ_g as the tensile forces are higher at same level of curvature. Figure 16c shows considerable increases in moment capacity as μ increases from 0 (brittle matrix) to 1 (elastic-perfectly plastic matrix). Note that the internal confinement role of fibers in the improvement of concrete compressive behavior is ignored in this analysis. Nevertheless, it can be incorporated simply by imposing confined compression model of concrete matrix.⁴⁶ Similar trends of concrete plasticity behavior are also observed.

As shown in Figure 16b,d, the normalized secant stiffness K' of HRC section is larger than 1.0 in uncracked range ($\phi' < 1.0$) as the cracking moment and curvature are estimated from plain concrete. Figure 16b shows that for a constant $\mu = 0.33$, postcracking stiffness in HRC section is efficiently enhanced by increasing ρ_g . On the other hand, when ρ_g is fixed, the stiffness degradation in the stage of deflection hardening is mitigated as μ increases from 0 to 1, which can be explained by the crack bridging through the depth by adding fibers.

Figure 16e compares the normalized moment-curvature diagrams for four levels of yield strength 235 MPa, 420 MPa, 550 MPa, and 690 MPa. It is observed that the f_{sy} directly affects the transition point of moment-curvature response into plateau stages, while the flexural stiffness is unchanged. The onset of plasticity of concrete in compression are also affected by the yield strength of steel. As shown in Figure 16f, positive effects of yielding strength on

Study	f'_c (MPa)	ρ (%)	v_f (%)	Service (%)	Ultimate (%)
Gribniak et al. (2012)	50.9	0.3	0	70.1	5.8
	55.6		0.5	43.1	-8.1
	48		1.0	11.2	-5.3
	52.2		1.5	0.3	0.8
Gribniak et al. (2013)	48.1	0.6	0	5.8	-13.4
	56	0.6 (GFRP)	1	-1.2	-2.7
	56	0.6 (GFRP)	1	-4.2	-1.0
Oh (1992)	40.3	1.84	0	-5.6	-9.9
	43.0		1	-11.4	-22.3
	47.8		2	-7.1	-22.7
	40.3	2.65	0	3.1	-21.3
	43.0		1	-1.5	-24.0
	47.8		2	11.4	-10.4
Yang et al. (2010)	192.2	0.60	2	17.2	-7.3
	196.1	0.90		14.1	3.0
Qiu et al. (2020)	131.6	0.73	2	-20.8	-2.0
		1.14		-4.3	-1.1
Qi et al. (2016)	116	4.96	2	13.9	-25.9
Abdul-Ahad and Aziz (1999)	18.8	2.09	2	-11.9	-14.1

TABLE 5 Prediction errors of the present model

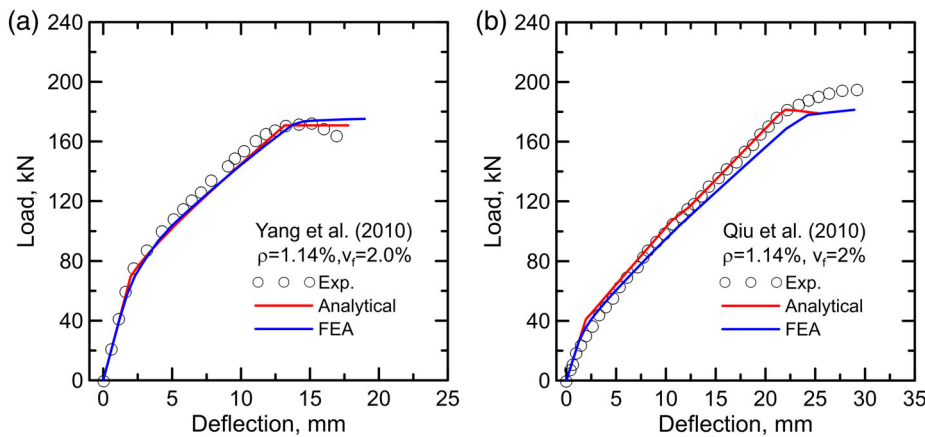


FIGURE 15 Model validation with FE analysis on the load-deflection curves from (a) Yang et al.⁴¹ and (b) Qiu et al.⁴⁴

retention of flexural stiffness are demonstrated. The rate of degradation was same until the steel yielded.

For HRC materials with T-section, effects of μ and ρ_g are found to be similar to those of rectangular section.³⁸ Therefore, geometrical parameters α and ζ are investigated for the T-section, as shown in Figure 17. Since all the parameters defining the cracking moment M_{cr} , and non-dimensional moment term are related to the material properties, geometry and loading conditions, moment-curvature response curves are generated using a

cross section parameters of $b = 500$ mm, $d = 600$ mm, with $\mu = 0.33$ and $\rho_g = 0.015$ (other material parameters remain the same). The two ratios α and ζ are varied from 0.1 to 0.3. The moment capacities increase by as much as 90% while different mechanisms are operational. The primary role of ζ is the improvement of postcracking stiffness by providing additional compression force, while its effect on cracking moment is non-existent. On the other hand, as α increases from 0.1 to 0.3, M_{cr} almost doubles, which agrees with the trend shown in.³⁸

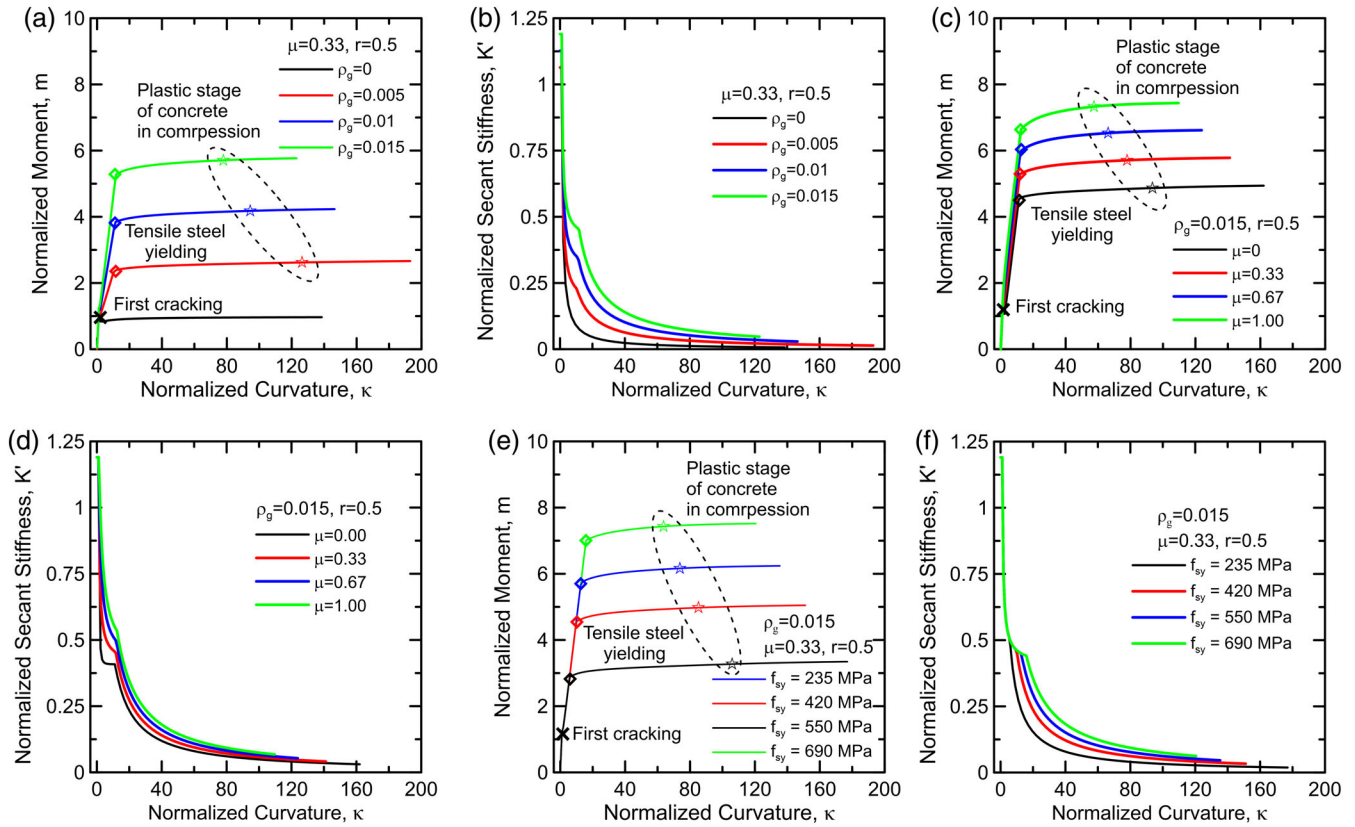


FIGURE 16 Normalized moment–curvature and stiffness degradation with changing parameters of (a) and (b) reinforcement ratio ρ_g , (c) and (d) normalized residual strength μ , and (e) and (f) steel yielding strength f_{sy}

FIGURE 17 Effects of geometrical parameters (a) normalized web thickness ϕ and (b) normalized flange height ζ on normalized moment–curvature responses

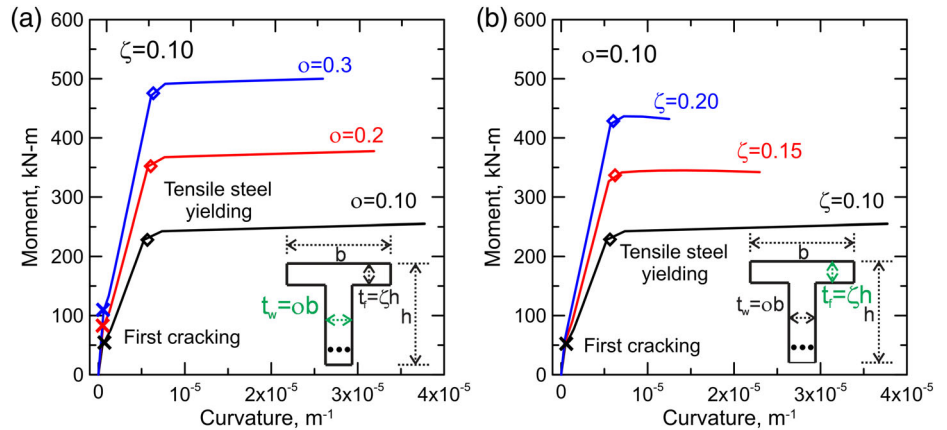


Figure 18 shows the interaction of two primary reinforcing parameters ρ_g and μ , in terms of the normalized moment. Two levels of moment were selected including the moment at yielding m_{ult} ($\kappa = \kappa_p$) and an intermediate level of curvature m_{int} ($\kappa = 0.5\kappa_p$). To better reveal the interactions, the maximum value of ρ_g was extended to 0.03, while μ still varied from 0 to 1. Other model parameters were kept same. It is

clearly observed that both parameters positively affect the flexural capacity, as shown in Figure 18a,b. To quantitatively investigate the increases of normalized moment caused by each parameter, the moment values obtained at $\rho_g = 0$ or $\mu = 0$ were subtracted from the moment response, which are plotted in Figure 18c,d. It can be seen that ρ_g exhibits more pronounced role in improving m_{ult} compared with m_{int} at

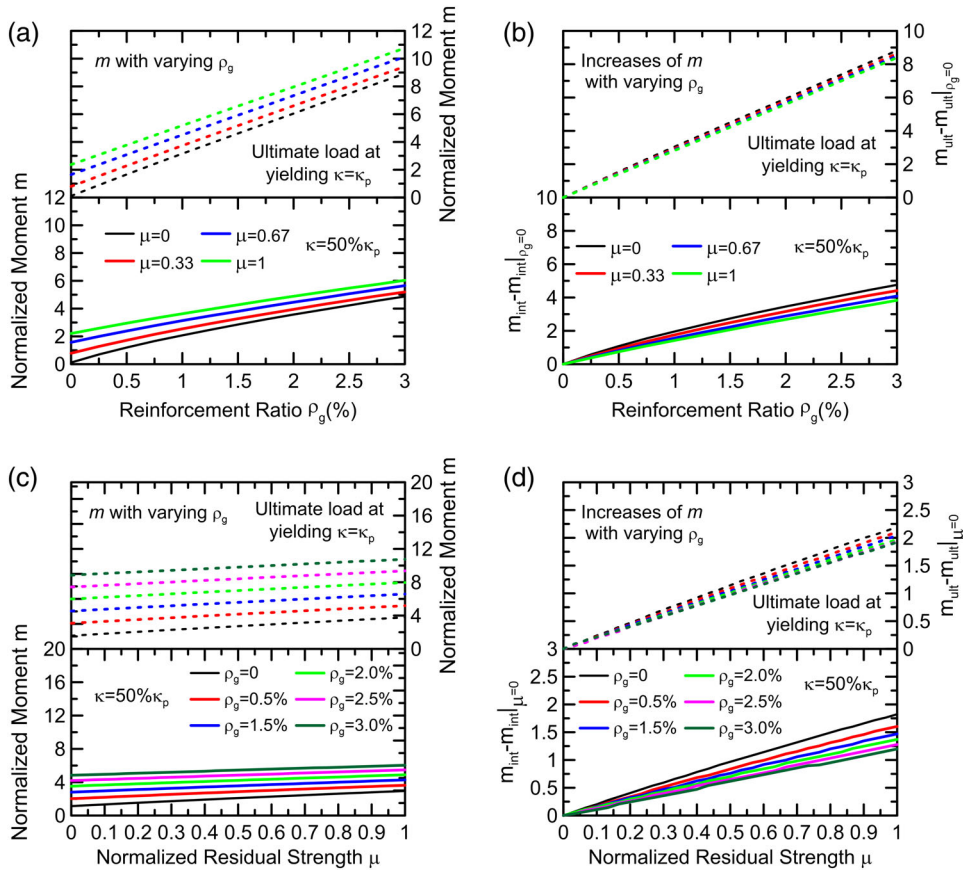


FIGURE 18 Interactions of reinforcement ratio ρ_g and normalized residual strength μ at intermediate and ultimate load levels in terms of (a) normalized moment and (b) increases of moment with varying ρ_g , (c) normalized moment and (d) increases of moment with varying μ

same (Figure 18c), since m_{ult} is dominated by the mechanical properties of steel bars. As μ increases from 0 to 1, the effect of ρ_g is reduced at intermediate load while the influence is marginal at ultimate state. This could be explained by the fiber bridging mechanisms at intermediate load levels such that the flexural load is partially carried by the fibers across the cracks. As the cracks widely open at ultimate stage, the role of fibers is diminished. Figure 18d shows the variance of m_{int} and m_{ult} at selected levels of ρ_g . The effects μ at ultimate state are more notable than intermediate load level but the differences are smaller compared to the effects of ρ_g . Similarly, as ρ_g increases from 0 to 0.03, the efficiency of μ also reduces. It may be explained by the reduced crack widths due to higher reinforcement ratio, such that the contribution of fiber bridging is decreased. Therefore, the selecting of reinforcing materials in practical design needs to consider their interactions at service and ultimate load levels to achieve optimal performance with minimal use of materials. This set of analysis may be useful for this purpose by generating design charts or tables for load or displacement, which applies to extended combinations of ρ_g and μ . In addition, the design chart can also be constructed as interaction of any other material

properties such as steel yielding strength and concrete compressive strength.

6 | SUMMARY AND CONCLUSIONS

An analytical model to predict the moment–curvature and load–deflection solutions was proposed for hybrid reinforced UHPC sections that takes the contributions and interactions of continuous reinforcements and discrete fibers into account. Parameterized constitutive models of the materials are incorporated for the derivation of full-range closed-form solutions including depth of neutral axis, moment and curvature as functions of various material parameters. Formulas of balanced reinforcement ratio and ultimate moment capacity were derived in analytical form. The present analysis method was also applied to T-section with hybrid reinforcement and analytical solutions for flexural behavior were obtained. The analytical solutions have been compiled and implanted in the form of excel spreadsheet-based programs. The user guide and the programs are available online^{23,47} and a brief introduction is presented in the supplemental materials.

The load–deflection response was obtained by two methods including numerical integration and analytical derivations. The analytical load–deflection solutions were derived based on a parameterized tri-linear moment–curvature curve that was after a linearization process. The derived solutions of displacement fields can be applied to the moment–curvature relationships obtained by the present approach on rectangular and T-sections or any other cross section analysis programs and customized sections.

Distributions of strain, stress and deflection were generated at specific levels of load which related the constitutive material models to the flexural behavior of the structural members. By following the same path, design charts in terms of deformation envelope or continuous response surfaces at desired level of serviceability states can be constructed for the selection of design parameters, which reflects the interactions of model parameters of interest. These design charts may be used to implement the serviceability-based design approach for reinforced UHPC members under flexure.

The proposed methodology was validated with a wide range of experimental data from literature for various materials and sections. The model was able to predict the flexural behavior of both normal strength concrete and hybrid reinforced UHPC members. According to the error analysis, deflections were underestimated for flexural members with higher reinforcement ratio, which might be explained by the fact that debonding of steel bars was not considered in the proposed model. However, overestimation was observed at service load level when reinforcement ratio and fiber dosage were both low. The phenomenon could be traced back to the tension model with drop-down residual strength which lead to sudden decreases after cracking under flexural load.

Parametric studies were conducted to investigate the effects of primary reinforcing and geometrical parameters. It was found that the reinforcement ratio ρ_g , yield strength of steel bars f_{sy} and normalized residual tensile strength μ positively affected the flexural performances of UHPC members. The analysis of interactions between ρ_g and μ revealed that the effects of fiber addition was more pronounced at intermediate load level but diminished at ultimate load that was dominated by steel yielding. The reducing efficiency of steel fiber was also observed with increasing reinforcement ratio which may be explained by less significant role of fiber bridging at reduced crack widths. By considering the interactions of reinforcing mechanisms, the proposed model may be useful in selection of design parameters to achieve optimal performance with minimal use of materials.

ACKNOWLEDGMENTS

This study was supported by the Natural Science Foundation of China (51908120), the Natural Science Foundation of Jiangsu Province (BK20180383) and the Fundamental Research Funds for the Central Universities (2242019K40079, 2242020K40099). The financial supports are gratefully appreciated.

NOTATION

A_s	area of tension steel
A_s'	area of compression steel
b	beam width
A_{1-7}, B_{1-11}	coefficients in Table 1
C_{1-8}, D_{1-9}	coefficients in Table 2
E_{1-8}, F_{1-9}	
d	effective depth at location of steel bar
E	elastic tensile modulus of concrete
E_c	elastic compressive modulus of concrete
E_s	elastic modulus of steel
f_c'	compressive strength of concrete
f	stress
f_s	steel stress
f_{sy}	steel yield stress
F	force components in stress diagram
G_1, G_2	coefficients for minimum flexural reinforcement in Equation (10)
h	full height of a beam section or height of each compression and tension zone in stress diagram
I	moment of inertia
I_{cr}	moment of inertia of cracked section
K	secant flexural stiffness of a beam section
k	neutral axis depth ratio
L	beam span
L_e	length of uncracked region in a beam
L_p	characteristic length
l_{cs}	crack spacing
M	moment
M_{cr}	moment at first cracking
M_p	moment at beginning of plastic stage
m	normalized moment (M/M_{cr})
m_p	normalized moment at beginning of plastic stage
n	modulus ratio (E_s/E)
r	ratio of compression steel to tension steel (A_s'/A_s)
t_f	flange height of T-section
t_w	web width of T-section
y	moment arm from force component to neutral axis
α	normalized depth of steel reinforcement (d/h)

β	normalized tensile strain ($\varepsilon_t/\varepsilon_{cr}$)
β_{tu}	normalized ultimate tensile strain ($\varepsilon_{tu}/\varepsilon_{cr}$)
ε	strain
ε_c	concrete compressive strain
ε_{cr}	concrete cracking strain
ε_{cu}	ultimate concrete compressive strain
ε_{ctop}	concrete compressive strain at top fiber
ε_s	steel strain
ε_{sy}	steel yield strain
ε_t	concrete tensile strain
ε_{tbot}	concrete tensile strain at bottom fiber
ε_{tu}	ultimate concrete tensile strain
φ	curvature
φ_{cr}	curvature at first cracking
φ_{max}	maximum curvature
θ	angle of rotation
γ	normalized concrete compressive modulus (E_c/E)
η	normalized postcracked flexural stiffness (EI_{cr}/EI_g)
κ	normalized curvature (φ/φ_{cr})
κ_p	normalized curvature at beginning of plastic stage
κ_{max}	normalized maximum curvature ($\varphi_{max}/\varphi_{cr}$)
λ	normalized compressive strain ($\varepsilon_c/\varepsilon_{cr}$)
λ_{R1}	normalized compressive strain corresponding to first cracking
λ_{cu}	ultimate concrete compressive strain ($\varepsilon_{cu}/\varepsilon_{cr}$)
μ	normalized residual tensile strength (σ_p/σ_{cr})
ρ	steel reinforcement ratio per effective area
ρ_g	steel reinforcement ratio per gross area
$\rho_{g,bal}$	steel reinforcement ratio per gross area at balanced failure
σ	concrete stress
σ_c	concrete compressive stress
σ_{cr}	concrete cracking stress
σ_{cy}	concrete compressive strength
σ_p	residual tensile strength
σ_t	concrete tensile stress
ν	Poisson's ratio
ω	normalized concrete compressive yield strain ($\varepsilon_{cy}/\varepsilon_{cr}$)
χ	normalized steel strain ($\varepsilon_s/\varepsilon_{cr}$)
ζ	normalized flange height (t_f/h)
o	normalized web thickness (b_w/b)
ψ	normalized steel yield strain ($\varepsilon_{sy}/\varepsilon_{cr}$)

SUBSCRIPTS

$t1, t2, t3$	tension zone 1, 2, 3
$c1, c2$	compression zone 1, 2
1,	Stage 1, 2.1, 2.2, 3.1, 3.2 according to the
21, 22, 31, 32	value of λ
Superscripts'	normalized parameters if not specified

ORCID

Yiming Yao  <https://orcid.org/0000-0002-5751-8180>

Barzin Mobasher  <https://orcid.org/0000-0002-7580-2855>

REFERENCES

1. Facconi L, Minelli F, Plizzari G. Steel fiber reinforced self-compacting concrete thin slabs – Experimental study and verification against Model Code 2010 provisions. *Eng Struct*. 2016;122:226–237. <https://doi.org/10.1016/j.engstruct.2016.04.030>.
2. Abbas S, Soliman AM, Nehdi ML. Chloride ion penetration in reinforced concrete and steel fiber-reinforced concrete precast tunnel lining segments. *Mater J*. 2014;111:613–622.
3. Briffaut M, Benboudjema F, D'Aloia L. Effect of fibres on early age cracking of concrete tunnel lining. Part II: Numerical simulations. *Tunn Undergr Space Technol*. 2016;59:221–229. <https://doi.org/10.1016/j.tust.2016.08.001>.
4. Deluce JR, Vecchio FJ. Cracking behavior of steel fiber-reinforced concrete members containing conventional reinforcement. *Struct J*. 2013;110:481–490.
5. Facconi L, Plizzari G, Minelli F. Elevated slabs made of hybrid reinforced concrete: Proposal of a new design approach in flexure. *Struct Concr*. 2019;20:52–67. <https://doi.org/10.1002/suco.201700278>.
6. Le Hoang A, Fehling E. Influence of steel fiber content and aspect ratio on the uniaxial tensile and compressive behavior of ultra high performance concrete. *Construct Build Mater*. 2017;153:790–806. <https://doi.org/10.1016/j.conbuildmat.2017.07.130>.
7. Yoo D-Y, Banthia N. Mechanical properties of ultra-high-performance fiber-reinforced concrete: A review. *Cem Concr Compos*. 2016;73:267–280. <https://doi.org/10.1016/j.cemconcomp.2016.08.001>.
8. Chen S, Zhang R, Jia L-J, Wang J-Y. Flexural behaviour of rebar-reinforced ultra-high-performance concrete beams. *Mag Concr Res*. 2017;70:997–1015. <https://doi.org/10.1680/jmacr.17.00283>.
9. Barros JAO, Taheri M, Salehian H. A model to simulate the moment–rotation and crack width of FRC members reinforced with longitudinal bars. *Eng Struct*. 2015;100:43–56. <https://doi.org/10.1016/j.engstruct.2015.05.036>.
10. di Prisco M, Plizzari G, Vandewalle L. Fibre reinforced concrete: New design perspectives. *Mater Struct*. 2009;42:1261–1281. <https://doi.org/10.1617/s11527-009-9529-4>.
11. Soranakom C, Mobasher B. Correlation of tensile and flexural responses of strain softening and strain hardening cement composites. *Cem Concr Compos*. 2008;30:465–477. <https://doi.org/10.1016/j.cemconcomp.2008.01.007>.

12. Vandewalle L. RILEM TC162-TDF: Test and design methods for steel fibre reinforced concrete: Bending test (final recommendation). *Mater Struct.* 2002;35:579–582.
13. Gribniak V, Kaklauskas G, Hung Kwan AK, Bacinskas D, Ulbinas D. Deriving stress-strain relationships for steel fibre concrete in tension from tests of beams with ordinary reinforcement. *Eng Struct.* 2012;42:387–395. <https://doi.org/10.1016/j.engstruct.2012.04.032>.
14. Svatopluk D, Gilles C. Inverse analysis tailored for UHPFRC. *J Eng Mech.* 2017;143:04017102. [https://doi.org/10.1061/\(ASCE\)EM.1943-7889.0001335](https://doi.org/10.1061/(ASCE)EM.1943-7889.0001335).
15. Xia J, Chan T, Mackie KR, Saleem MA, Mirmiran A. Sectional analysis for design of ultra-high performance fiber reinforced concrete beams with passive reinforcement. *Eng Struct.* 2018; 160:121–132. <https://doi.org/10.1016/j.engstruct.2018.01.035>.
16. Soranakom C, Mobasher B. Closed-form solutions for flexural response of fiber-reinforced concrete beams. *J Eng Mech.* 2007; 133:933–941. [https://doi.org/10.1061/\(ASCE\)0733-9399\(2007\)133:8\(933\)](https://doi.org/10.1061/(ASCE)0733-9399(2007)133:8(933)).
17. Yao Y, Aswani K, Wang X, Mobasher B. Analytical displacement solutions for statically determinate beams based on a trilinear moment-curvature model. *Struct Concr.* 2018;16:1619–1632. <https://doi.org/10.1002/suco.201700150>.
18. Shafieifar M, Farzad M, Azizinamini A. A comparison of existing analytical methods to predict the flexural capacity of ultra high performance concrete (UHPC) beams. *Construct Build Mater.* 2018;172:10–18. <https://doi.org/10.1016/j.conbuildmat.2018.03.229>.
19. Mobasher B, Yao Y, Soranakom C. Analytical solutions for flexural design of hybrid steel fiber reinforced concrete beams. *Eng Struct.* 2015;100:164–177. <https://doi.org/10.1016/j.engstruct.2015.06.006>.
20. van Zijl GPAG, Mbewe PBK. Flexural modelling of steel fibre-reinforced concrete beams with and without steel bars. *Eng Struct.* 2013;53:52–62. <https://doi.org/10.1016/j.engstruct.2013.03.036>.
21. Mobasher B, Yao Y, Soranakom C, Dey V. (2015) A spreadsheet-based inverse analysis procedure for flexural specimens – Strain softening/hardening behavior. ResearchGate <https://doi.org/10.13140/RG.2.1.4409.2882>
22. Yao Y, Bakhshi M, Nasri V, Mobasher B. (2018) A spreadsheet-based analytical procedure for design of hybrid fiber reinforced concrete tunnel lining segments. ResearchGate <https://doi.org/10.13140/RG.2.2.14437.09440>
23. Mobasher B, Yao Y, Soranakom C. (2020) A spreadsheet-based analytical procedure for design of hybrid reinforced concrete flexural members. ResearchGate <https://doi.org/10.13140/RG.2.2.32125.72167>
24. Casanova P, Rossi P. Analysis and design of steel fiber reinforced concrete beams. *Struct J.* 1997;94:595–602.
25. Amin A, Foster SJ, Kaufmann W. Instantaneous deflection calculation for steel fibre reinforced concrete one way members. *Eng Struct.* 2017;131:438–445. <https://doi.org/10.1016/j.engstruct.2016.10.041>.
26. Buratti N, Ferracuti B, Savoia M. Concrete crack reduction in tunnel linings by steel fibre-reinforced concretes. *Construct Build Mater.* 2013;44:249–259. <https://doi.org/10.1016/j.conbuildmat.2013.02.063>.
27. Oh BH. Flexural analysis of reinforced concrete beams containing steel fibers. *J Struct Eng.* 1992;118:2821–2835. [https://doi.org/10.1061/\(ASCE\)0733-9445\(1992\)118:10\(2821\)](https://doi.org/10.1061/(ASCE)0733-9445(1992)118:10(2821)).
28. DAfStb (2012) Richtlinie Stahlfaserbeton/Technical Guidelines for Steel Fiber Reinforced Concrete, part 1–3, “Deutscher Ausschuss für Stahlbeton (DAfStb) im DIN Deutsches Institut für Normung/German Association for Reinforced Concrete within DIN.
29. CNR, DT. 204/2006 (2006) Guidelines for the design, construction and production control of fibre reinforced concrete structures.
30. EHE-08. Spanish code on structural concrete—Annex 14: Recommendations for using concrete with fibres. Madrid, Spain: Ministry of Public Works and Transport, 2008.
31. fib – federation internationale du beton (2013) fib Model Code for Concrete Structures. Lausanne, Switzerland: Ernst & Sohn, 2010.
32. 544.8R-16: Report on Indirect Method to Obtain Stress-Strain Response of Fiber-Reinforced Concrete (FRC). <https://www.concrete.org/store/productdetail.aspx?ItemID=544816>. Accessed 10 August 2017
33. ASTM C1609 (2019) ASTM C1609/C1609M – 19a standard test method for flexural performance of fiber-reinforced concrete (using beam with third-point loading). ASTM Int West Conshohocken PA.
34. Barros JAO, Cunha VMCF, Ribeiro AF, Antunes JAB. Post-cracking behaviour of steel fibre reinforced concrete. *Mater Struct.* 2005;38:47–56. <https://doi.org/10.1007/BF02480574>.
35. Qian S, Li VC. Simplified inverse method for determining the tensile strain capacity of strain hardening cementitious composites. *J Adv Concr Technol.* 2007;5:235–246. <https://doi.org/10.3151/jact.5.235>.
36. Graybeal BA. Structural behavior of a 2nd generation UHPC pi-girder. Washington DC: Federal Highway Administration (FHWA); 2009.
37. di Prisco M, Dozio D, Belletti B. On the fracture behaviour of thin-walled SFRC roof elements. *Mater Struct.* 2013;46: 803–829. <https://doi.org/10.1617/s11527-012-9935-x>.
38. Yao Y. Characteristics of distributed cracking for analysis and design of strain hardening cement based composites [PhD dissertation]. Arizona State University; 2016.
39. Wang X. Analytical load-deflection equations for beam and 2-D panel with a bilinear moment-curvature model. ASU Electronic Dissertations and Theses. Arizona State University; 2015.
40. Gribniak V, Kaklauskas G, Torres L, Daniunas A, Timinskas E, Gudonis E. Comparative analysis of deformations and tension-stiffening in concrete beams reinforced with GFRP or steel bars and fibers. *Compos B Eng.* 2013;50:158–170. <https://doi.org/10.1016/j.compositesb.2013.02.003>.
41. Yang IH, Joh C, Kim B-S. Structural behavior of ultra high performance concrete beams subjected to bending. *Eng Struct.* 2010;32:3478–3487. <https://doi.org/10.1016/j.engstruct.2010.07.017>.
42. Abdul-Ahad RB, Aziz OQ. Flexural strength of reinforced concrete T-beams with steel fibers. *Cem Concr Compos.* 1999;21: 263–268. [https://doi.org/10.1016/S0958-9465\(99\)00009-8](https://doi.org/10.1016/S0958-9465(99)00009-8).
43. Qi J-N, Ma ZJ, Wang J-Q, Liu T-X. Post-cracking shear strength and deformability of HSS-UHPFRC beams. *Struct Concr.* 2016; 17:1033–1046. <https://doi.org/10.1002/suco.201500191>.

44. Qiu M, Shao X, Wille K, Yan B, Wu J. Experimental investigation on flexural behavior of reinforced ultra high performance concrete low-profile T-beams. *Int J Concr Struct Mater.* 2020; 14:1–20. <https://doi.org/10.1186/s40069-019-0380-x>.
45. Zhang Z, Shao X, Zhu P. Direct tensile behaviors of steel-bar reinforced ultra-high performance fiber reinforced concrete: Effects of steel fibers and steel rebars. *Constr Build Mater.* 2020;243. <https://doi.org/10.1016/j.conbuildmat.2020.118054>.
46. Yao Y, Bakhshi M, Nasri V, Mobasher B. Interaction diagrams for design of hybrid fiber-reinforced tunnel segments. *Mater Struct.* 2018;51:35. <https://doi.org/10.1617/s11527-018-1159-2>.
47. Mobasher B, Bakhshi M, Barsby C, et al. (2015) Model user guide. ResearchGate <https://doi.org/10.13140/RG.2.2.16011.80162>

AUTHOR BIOGRAPHIES



Yiming Yao,
School of Civil Engineering,
Southeast University,
Nanjing, PR China.
Email: yiming.yao@seu.edu.cn



Barzin Mobasher,
School of Sustainable Engineering
and Built Environment,
Arizona State University,
Tempe, AZ, USA.
Email: barzin@asu.edu



Jingquan Wang,
School of Civil Engineering,
Southeast University,
Nanjing, PR China.
Email: wangjingquan@seu.edu.cn



Qizhi Xu,
School of Civil Engineering,
Southeast University,
Nanjing, PR China.
Email: 230179095@seu.edu.cn

SUPPORTING INFORMATION

Additional supporting information may be found online in the Supporting Information section at the end of this article.

How to cite this article: Yao Y, Mobasher B, Wang J, Xu Q. Analytical approach for the design of flexural elements made of reinforced ultra-high performance concrete. *Structural Concrete.* 2020; 1–20. <https://doi.org/10.1002/suco.201900404>